28th Symposium on Naval Hydrodynamics
Pasadena, California, 12-17 September 2010

Effects of Polymer Injection on Vortex Cavitation Inception

C.-T. Hsiao, Q. Zhang, X. Wu and G. L. Chahine
(DYNAFLOW, INC., USA)

ABSTRACT
The effects of polymer injection on vortex cavitation inception were studied both numerically and experimentally. For the numerical study, a FENE-P model was implemented in the Navier-Stokes solver, 3DYNAFS-VIS©, to simulate viscoelastic effects of polymer solutions on tip vortex cavitation. This model was applied to simulate the tip vortex flow generated by an open propeller in water and polymer solutions. The pressure along the vortex centerline was found to be higher for the polymer solution than for water. This implies that the presence of polymer makes cavitation more difficult to occur. Experimentally, a vortex chamber with a polymer injection port on the axis was designed to study the effect of local polymer injection on cavitation inception. The injection flow rate and polymer concentration required to delay cavitation in the vortex core were investigated for different vortex strengths. In addition, PIV measurements of the flow field inside the vortex chamber were used to provide data for the viscoelastic model validation.

1. Introduction

Navies have devoted great efforts to delaying tip vortex cavitation (TVC) inception. Previous studies have found that TVC can be efficiently delayed by injecting dilute polymer solutions from the blade tip. Fruman and Aflalo (1989) reported that for an elliptic hydrofoil, the injection of the polymer solution increases the tip vortex radius as well as reduces the tangential velocity. Chahine *et al.* (1993) investigated the TVC for a rotating propeller with the injection of Polyox WSR301 solutions as well as with water/glycerin mixtures. They found, using very low flow rates of injection, that the cavitation inception number can be decreased by as much as 35% with polymer injection, while under the same conditions a water/glycerin mixture does not affect the inception characteristics in an appreciable fashion. The differences in performances of the polymer solution and in a Newtonian fluid were investigated later by Fruman *et al.* (1995). These studies imply that the viscoelastic properties of the injected solution into the vortex core are responsible for the useful effect.

However, the fundamental mechanisms of modification of the tip vortex flow and cavitation are not fully understood. Experimental measurements of the velocity in the tip vortex core region of a rotating propeller are very challenging due to both the rotation motion and the wandering of the vortex core. Even for a tip vortex flow generated by a fixed finite-span foil, the location of polymer injection influences significantly the results. To study the problem in a better controlled laboratory environment, we built a Plexiglas vortex chamber to generate and visualize a line vortex flow. A centered injection was designed to inject the polymer solutions directly into the vortex center.

In parallel to the experimental study, we are conducting a numerical study to better understand the flow structure modification due to the polymers. Non-Newtonian features of a polymer solution include many aspects, such as shear-thinning effect, memory effects, stretching-induced normal stress effect, etc. Previous researchers have built up models accounting for these effects, for example Bird et al. (1987), and several numerical approaches to model viscoelasticity were investigated to study polymer solution effects on flows, especially those resulting in drag reduction (see e.g. Li et al. 2006, Oliveira et al. 1998). Among these studies, the FENE-P (Finite-Extensibility-Nonlinear-Elasticity Peterlin) model is now widely used because it can model well the rheological properties of a long-chain polymer solution such as Polyox WSR 301. Although there are competing models (e.g. FENE, Oldroyd-B), the FENE-P model is preferred because it accounts for the finite extensibility of the molecules and uses a simple second-order closure model in the equation for the polymer stress tensor. Finite extensibility is physically consistent with the polymers physics and also helps numerical stability. The use of the second order closure-model reduces computational

costs as commented in a recent review by White and Mungal (2008). Therefore, we have implemented FENE-P model in our Navier-Stokes solver, 3DYNAFS_VIS©, to investigate polymer effects on vortex flows.

2. Experimental Study in a Vortex Chamber

2.1 Experimental Setup

Experiments were conducted in a vortex chamber that consisted of two concentric cylinders. End plates with circular orifice openings were mounted on each end-side of the cylinders to close the chamber. A larger orifice at one end served as flow outlet, while a small orifice at the other end was used for polymer injection. The flow was brought into the outer cylinder along a tangential direction in the mid-section between the two end plates. Figure 1 shows a drawing of the vortex chamber assembly as well as the coordinate definition. Table 1 gives the key dimensions of the chamber. Notice that there were four all-through slots on the inner chamber in this vortex chamber design. This was an improvement over the previous design, which used eight discrete short injection slots (Barbier et al 2009). The objective is to improve the steadiness of the cavitating core which was found unstable in the previous polymer experiments.

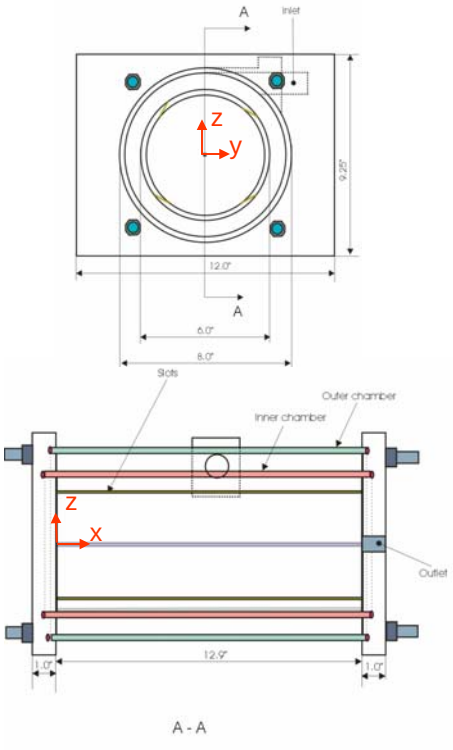

Figure 1: Dimensions of the vortex chamber assembly used for vortex cavitation inception studies.

Chamber length	12.9 in
Inner cylinder OD	6.0 in
Inner cylinder ID	5.5 in
Outer cylinder OD	8.0 in
Outer cylinder ID	7.5 in
Slot length	12.9 in
Slot height	0.078 in
Total number of slots	4
Angular positions of the slots	45^o, 135^o, 225^o, 315^o
Outlet orifice diameter	0.6 in
Injection orifice diameter	0.078 in
Tank liquid level	12 in
Outlet-tank wall distance	24 in

Table 1: List of key dimensions of the studied vortex chamber.

The vortex chamber was submerged in a long reservoir tank (14" x 14"x 40") filled with liquid and formed a close loop with a re-circulating pump. Figure 2 shows a schematic of the setup. As shown in the figure, the vortex chamber was off-centered in the tank such that the flow outlet of the chamber was away from the tank end to minimize disturbances to the vortex flow. Additionally, the liquid was supplied from the top of the chamber and was then taken out from the bottom of the tank near the other tank end such that it did not disturb the flow near the outlet of the swirl chamber.

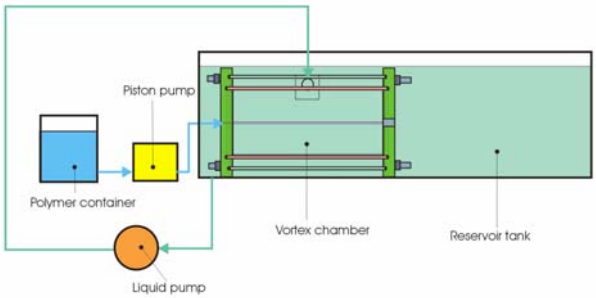

Figure 2: Schematic of the test loop used in the vortex cavitation inception studies.

The fluid entered first in the outer cylinder, which served as a plenum chamber, then was injected tangentially into the inner chamber through four end-to-end tangential slots. When the flow rate exceeded a limit value, cavitation occurred at the center of the vortex and as the flow increased a tubular cavitation vortex line was observed at the centerline of the cylinders between the two orifices (see Figure 3).

Polymer solutions were introduced into the vortex core through the injection orifice. A digital piston pump was used to pump the polymer solution at a preset injection rate. A high-speed camera and an HD

video camera were used for flow visualization of the polymer injection effects. A picture of the experimental setup is shown in Figure 4.

Figure 3: Picture of the vortex chamber with a cavitation core throughout.

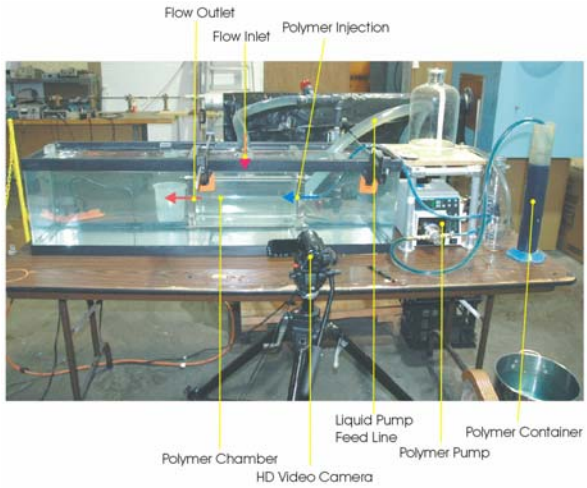

Figure 4. A snap shot of the experiment set up with polymer injection.

For flow field measurements, an Oxford laser VisiVector E6 PIV system was used to perform the Particle Image Velocimetry (PIV) measurements. This system employed a HSI diode laser (15 mJ/pulse, 808 nm wavelength). A combination of spherical and cylindrical lenses was used to produce a laser sheet 30 mm wide and 2 mm thick in the area of interest. The duration of a single laser pulse was 40-50 μs and the time between pulses ranged between 400 μs at low flow rates to 10 μs at high flow rates.

A PCO Pixelfly-qe CCD camera with an AF Nikkor (Nikon) 35mm f2.0D lens with a teleconverter x2 set at about 2-2.5 ft from the mid-plane of the chamber was used to capture the PIV images. The camera had a resolution of 1,392x1,024 pixel (12-bit digital output) at 12 frames per second and a field of view of 34 mm x 25 mm was achieved.

Since the field of view of the camera is much smaller than the flow field of interest, the camera was mounted on a 3D programmable motorized slide table that can move to a user specified position with a precision of 0.1 mm as shown in Figure 5. This allowed controlling the position of the PIV camera precisely.

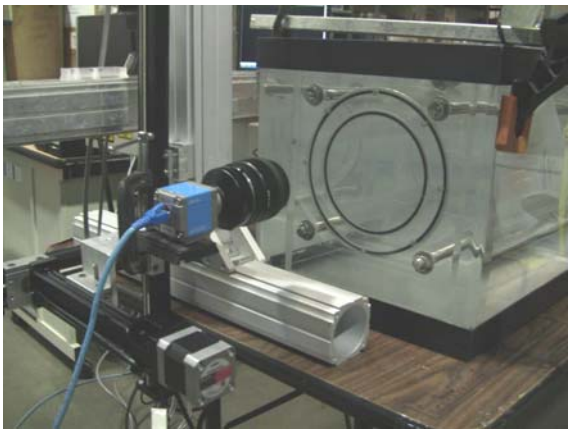

Figure 5. A snap shot of the PIV camera mounted on a 3D programmable motorized slide.

The commercial ViDPIV software was used for image acquisition and subsequent data processing. The calculations of instantaneous velocity vector maps were done by means of cross-correlation between two images. In a first pass, a standard cross-correlation function, including a Whitaker peak fit and phase correlation, was performed on interrogation windows; then a local median filter was applied, and the resulting filtered vectors interpolated. In a second pass, an adaptive cross-correlation method was applied on reduced interrogation windows, after applying a local median filter, and the resulting filtered vectors interpolated to fine tune the analysis. The adaptive cross-correlation procedures are repeated as many times as needed to achieve the quality of analysis required.

2.2 Effects of Polymer Injection

For the setup described here, a cavitation core was found to appear at about 12 gpm in pure water. Initially the cavitation core wandered around the chamber axis and cavitation appearance was intermittent across the chamber. As the flow rate increased, the cavitation became an end-to-end steady tubular core.

To study the effects of polymer injection on the cavitation core, polymer solutions made of Polyox at three concentrations, 1,000 PPM, 4,000 PPM, and 6,000 PPM were prepared. The polymer solution was

pumped into the core at a given constant injection rate through the injection orifice with an injection needle. The behaviour of the cavitation core was recorded and analyzed.

Figure 6 shows a typical sequence of cavitation core disappearance in response to the polymer injection: the core shrinks, detaches from the end plate, and disappears. The conditions for the above phenomenon to happen depend on the liquid flow rate as well as on the polymer solution injection rate.

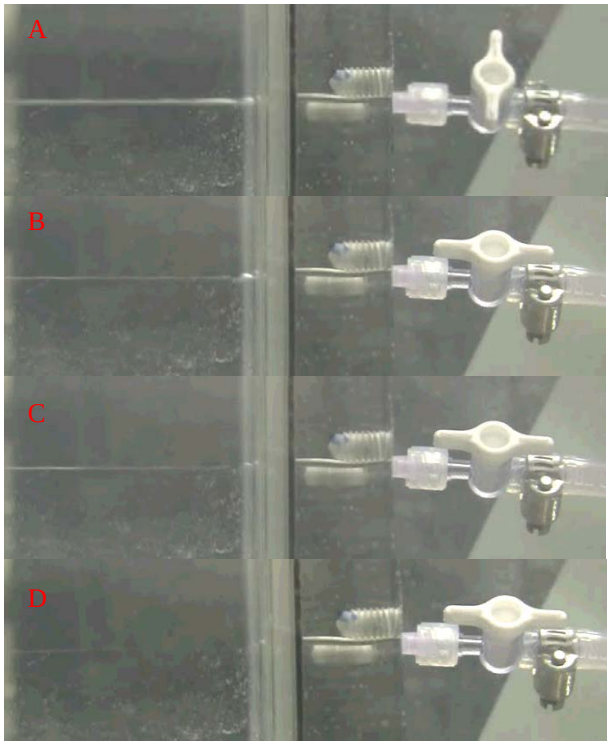

Figure 6: Response of cavitation core to polymer injection. Water flow rate 15 gpm. Polymer injection rate 500 ml/min. (A) Before polymer injection, (B) – (D), sequence of cavitation core shrinkage, detachment, and disappearance in response to the polymer injection.

Figure 7 shows the effects of polymer injection rate and concentration on the cavitation core behaviour at different flow rates. It is seen that the higher the water flow rate (or vortex circulation), the higher polymer injection rate is required to force cavitation core detachment from the end of the chamber and the cavitation to disappear. Also, the higher the polymer concentration, the lower injection rate is required at a given flow rate to achieve cavitation suppression.

After the cavitation core detached from the end of the polymer chamber, the core could remain downstream near the outlet orifice. For example, Figure 8 shows a snap shot of the cavitation core at two instants for the water flow rate of 17 gpm. It is seen that the length of the fluctuating cavitation core changes significantly as the polymer solution was injected to suppress cavitation. Figure 9 and Figure 10 show the measured time-accurate cavitation core length and time-averaged lengths respectively for different polymer injection rates. It is seen that both the amplitude of the fluctuations and the time-averaged length decrease as the polymer injection rate was increased.

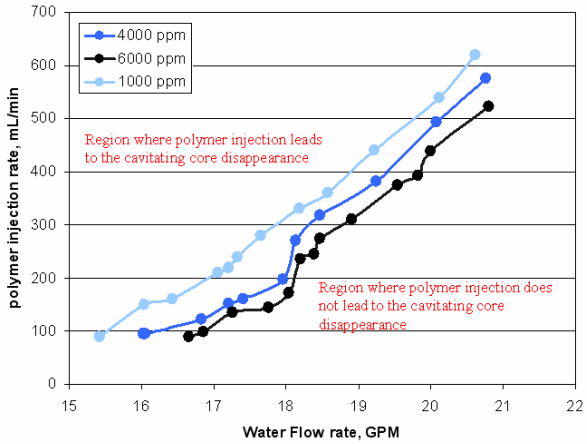

Figure 7. Effects of polymer concentration and injection rate on cavitation core suppression at various flow rates.

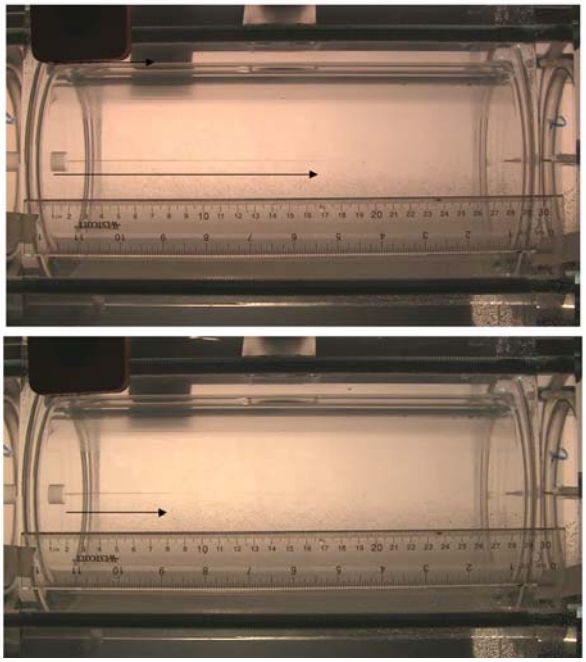

Figure 8. Snap shots showing the fluctuation of the detached cavitation core, the arrow indicates the core length. The flow rate was 17 gpm.

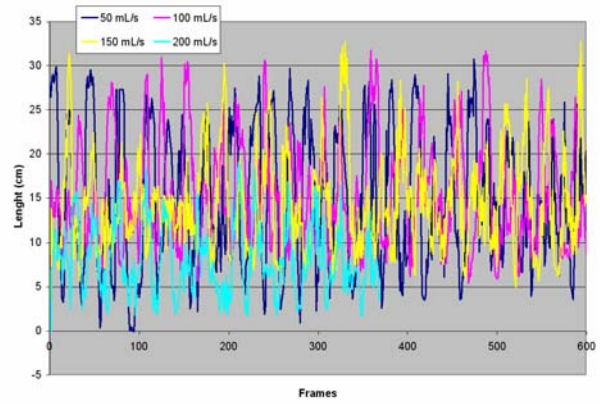

Figure 9: Cavitation core length fluctuation at different polymer injection rate for flow rate of 17 gpm.

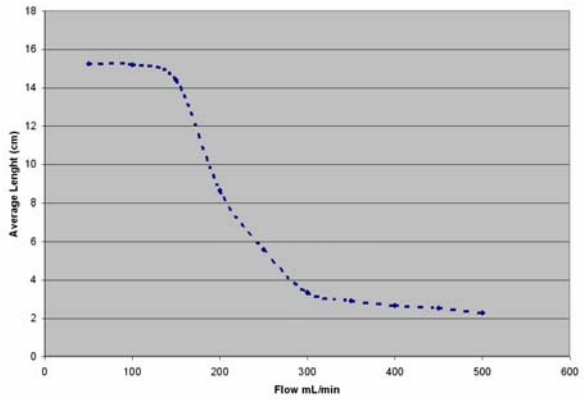

Figure 10: Variation of average cavitation core length with polymer injection rate for flow rate of 17 gpm.

Figure 11: Comparison of the cavitation without (top) and with injection of water into the cavitation core (bottom). The flow rate is 15 gpm and the injection rate is 2,000 ml/min.

For comparison purposes, injection of pure water was also studied. From experiments, we observed no significant influence of the water injection on the cavitation core and the cavitation core does not detach from the end wall of the vortex chamber as the water injection flow rate was small. However, the cavitation core became a helix shape and wandered around the chamber axis as the water injection rate was increased. Figure 11 shows the comparison of the cavitation core behavior with and without injection of water, the flow rate was 15 gpm and the injection rate of water is 2,000 ml/min.

2.3 Flow Field Measurements

Particle Image Velocimetry (PIV) measurements were also conducted to study the flow field of the swirling flow to provide for numerical validation. Three planes were selected across the chamber, at X = 1 cm (1 cm downstream from the injection orifice), X = 16.4 cm (the mid-plane of the vortex chamber), and X = 31.8 cm (1 cm upstream to the outlet orifice) respectively. In each measurement plane, 7 PIV measurements were conducted to produce full coverage of the area of interest. Figure 12 shows schematics of the arrangement of the three image planes on the swirl chamber and the field coverage in each measurement plane. The field coverage was selected such that the velocity profiles along the 0°, 45° and 90° could be extracted from the PIV measurements.

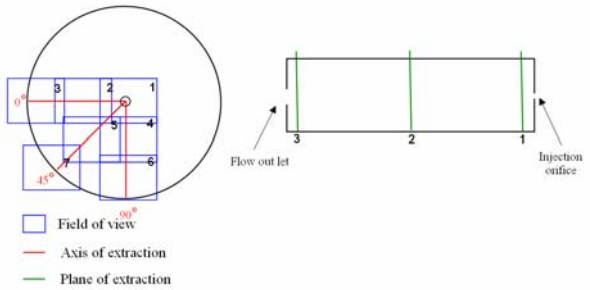

Figure 12: Locations of three PIV measurement planes and the field of view coverage of the 7 PIV measurements on each plane.

Figure 13 shows an example of the time fluctuations of the instantaneous velocity profiles along the 0° direction in the middle plane for 11 gpm. The peak w velocities varied by as much as 50% in this case. Figure 14 shows the time-averaged v and w velocity profiles in the mid-plane in the 0° direction for 11 gpm, both figures show similar profiles. The w velocity profiles had typical vortical flow velocity profiles, but the location of the zero velocity was not the same as the geometric center of the orifice and has a shift of about 2.5 mm, which may explain the fluctuations coupled with the wandering. Also for the averaged w velocities peaked around the y location

where the v velocity crossed zero but the w velocities do not cross zero which also indicates that the vortex center has a shift from the geometric center.

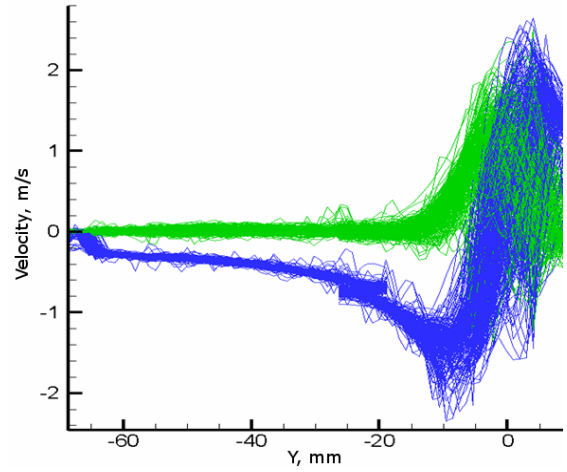

Figure 13: Fluctuations of the instantaneous velocities v (green lines) and w velocities (blue lines) profiles along the y direction .crossing (x = 16.4, z = 0).

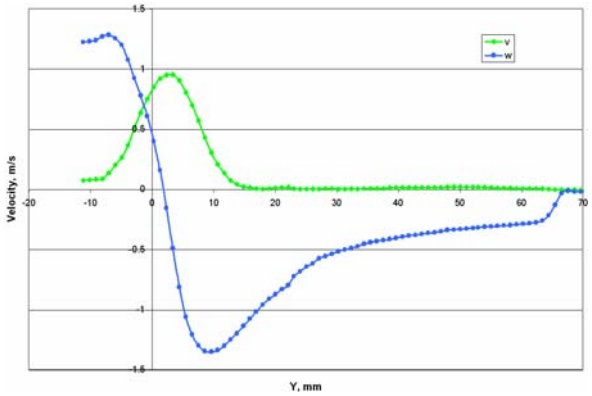

Figure 14: Averaged *v* and *w* velocity profiles along the y direction .crossing (x= 16.4, z = 0).

3. Numerical Study of Polymer Effects on Vortex Flows

3.1 Governing Equations

The flow of a dilute, homogeneous and incompressible polymer solution is described by the continuity and the momentum conservation momentum equations:

$$\nabla \bullet \mathbf{u} = 0\,, \tag{1}$$

$$\frac{D\mathbf{u}}{Dt} = -\nabla p + \frac{\beta}{\mathrm{Re}}\nabla^2\mathbf{u} + \frac{1-\beta}{\mathrm{Re}}\nabla \bullet \mathbf{T}\,, \tag{2}$$

where **u** represents the fluid velocity, *p* the pressure, *t* the time, and **T** the viscoelastic extra-stress tensor. Equations (1) and (2) are in non-dimensional form with a characteristic velocity, *U*, and characteristic length, *l*. The Reynolds number, $\mathrm{R_e}$, is based on *U*, *l* and the total viscosity, $\mu = \mu_s + \mu_p$, where μ_s is the solvent (water) viscosity and μ_p is the extra shear viscosity due to the polymer. The parameter β is the viscosity portion due to the solvent and is defined as $\beta = \mu_s / \mu$. The polymer stress is normalized by $\mu_p U / l$.

The polymer stress tensor T is related to the flow field strains through the constitutive equation of the Finitely Extensible Nonlinear Elastic - Peterline (FENE-P) dumbbell model (Bird et al. 1987):

$$\mathbf{T} = \frac{1}{D_e}\left(f\mathbf{c} - a\mathbf{I}\right), \tag{3}$$

where **c** is the conformation tensor, defined as the ensemble averaged dyad of the end-to-end distance of the polymer chains. D_e is the Deborah (or Weissenberg) number, which is the non-dimensional relaxation time λ of the polymer

$$D_e = \frac{\lambda}{l / U}\,, \tag{4}$$

and f is the Peterlin function

$$f = \frac{L^2}{L^2 - c_{kk}}\,, \tag{5}$$

where L is the extensibility parameter and c_{kk} is the trace of tensor **c**.

The equation for the conformation tensor c is governed by

$$\frac{D\mathbf{c}}{Dt} - \left(\nabla\mathbf{u}\bullet\mathbf{c} + \mathbf{c}\bullet\nabla\mathbf{u}^T\right) = -\frac{1}{D_c}\left(f\mathbf{c} - a\mathbf{I}\right), \tag{6}$$

in which the superscript '*T*' denotes the transpose. Since the conformation tensor **c** is symmetric, only 6 components are computed.

The parameter *a* depends on L as follows,

$$a = \frac{1}{1 - \dfrac{3}{L^2}}\,. \tag{7}$$

when $L \to \infty$, FENE-P model recovers the Oldroyd-B model. In this study, *L* is set to be 60, as used by Li et al. (2006).

The viscosity and the polymer stress will depend on the local polymer solution concentration, especially if the considered problem involves local polymer injection. In this case, a transport equation of the polymer concentration, ϕ, needs to be solved:

$$\frac{\partial\phi}{\partial t} + \mathbf{u}\bullet\nabla\phi = \frac{1}{S_c\,\mathrm{Re}}\nabla^2\phi\,, \tag{8}$$

where S_c is the Schmidt number defined by

$$S_c = \frac{\mu_s}{\rho D}, \tag{9}$$

in which D is the diffusion coefficient of the polymer molecules.

3.2 Numerical Scheme

To solve Equations (1) and (2), a three-dimensional incompressible Navier-Stokes solver, 3DYNAFS-VIS© is exercised. 3DYNAFS-VIS© includes in addition to the present viscoelastic model, a moving overset grid scheme for bubble dynamics problems, an Eulerian/Lagrangian two-way coupling scheme for simulation of bubble/liquid two phase flows, and a Level Set scheme for simulation of large-deformation free surface flows.

3DYNAFS-VIS© is based on the artificial-compressibility method (Chorin 1967), in which an artificial time derivative of the pressure is added to the continuity equation as

$$\frac{1}{\beta_c}\frac{\partial p}{\partial t} + \nabla \bullet \mathbf{u} = 0, \tag{10}$$

where β_c is the artificial compressibility factor. As a consequence, the hyperbolic system of equations (1) and (2) is formed and is solved using a time marching scheme in the pseudo-time to reach a steady-state solution. To obtain a time-dependent solution, a Newton iterative procedure is performed at each physical time step in order to satisfy the continuity equation.

The numerical scheme in 3DynaFS-Vis© uses a finite volume formulation and is based on the code UNCLE developed by Mississippi State University (Arabshahi et al. 1995). A first-order Euler implicit difference formula is applied to the time derivatives. The spatial differencing of the convective terms uses the flux-difference splitting scheme based on Roe's method (Roe 1981) and a van Leer's MUSCL method for obtaining the first- or third-order fluxes. A second-order central differencing is used for the viscous terms, which are simplified using the thin-layer approximation. The flux Jacobians required in an implicit scheme are obtained numerically. The resulting system of algebraic equations is solved using a discretized Newton Relaxation method in which symmetric block Gauss-Seidel sub-iterations are performed before the solution is updated at each Newton iteration.

In order to extend the Navier-Stokes solver to non-Newtonian fluids, a time integration scheme of Equation (6) to obtain the conformation tensor **c;** and thus the polymer stress tensor **T,** was implemented and coupled to the original NS solver. The solutions of the constitutive and momentum equations and polymer stress tensor **T** are staggered, i.e. the polymer contribution in Equation (2) is calculated at each step once the velocity is known, then equation (2) can be solved as the usual Navier-Stokes equation with a body force term from the divergence of the polymer stress.

At time step *n*, the velocity $\mathbf{u}^n$, the pressure p^n, and the polymer stress $\mathbf{T}^n$ are known. Using $\mathbf{u}^n$, Equation (6) can be integrated to provide the conformation tensor for the next time step. A first order differentiation in the time stepping, with time step Δt is used:

$$\frac{\mathbf{c}^{n+1} - \mathbf{c}^n}{\Delta t} = \left[-\mathbf{u}\bullet\nabla\mathbf{c} - \left(\nabla\mathbf{u}\bullet\mathbf{c} + \mathbf{c}\bullet\nabla\mathbf{u}^T \right) - \frac{1}{De}\left(f\mathbf{c} - a\mathbf{I} \right) \right]^n . \tag{11}$$

For the spatial discretization of Equation (11), a first order upwind scheme is used for the convection term and a second order center difference scheme is used for the velocity gradient. After obtaining $\mathbf{c}^{n+1}$, the polymer stress $\mathbf{T}^{n+1}$ is calculated from Equation (3) and the divergence of $\mathbf{T}$ is obtained. This provides the polymer stress term in Equation (2):

$$\mathbf{b}_{polymer} = \frac{1-\beta}{\mathrm{Re}}\nabla\bullet\mathbf{T}^{n+1}, \tag{12}$$

and the momentum equation at step *n*+1 becomes:

$$\frac{D\mathbf{u}^{n+1}}{Dt} = -\nabla p^{n+1} + \frac{\beta}{\mathrm{Re}}\nabla^2\mathbf{u}^{n+1} + \mathbf{b}_{polymer}, \tag{13}$$

which has the same form as the Newtonian Navier-Stokes equation.

Together with the continuity equation, Equation (13) is solved to get the velocity $\mathbf{u}^{n+1}$ and the pressure p^{n+1}. At this point, all the quantities for step *n*+1 are known and a new loop starts with the calculation of $\mathbf{c}^{n+2}$.

In addition to the time integration of Equation (6) , in the case of local polymer injection, we also need to solve Equation (8). Similar to solving Equation (11), the concentration equation is integrated at each time step once the velocity is known from the Navier-Stokes equations:

$$\frac{\phi^{n+1} - \phi^n}{\Delta t} = \left[-\mathbf{u}\bullet\nabla\phi + \frac{1}{Sc\,\mathrm{Re}}\nabla^2\phi \right]^n . \tag{14}$$

The convection term is discretized using the first order upwind and for the diffusion term a second order central difference scheme is used. In simulating the

local polymer injection problem, we have the Reynolds number, β, and D_e are locally dependent on ϕ as detailed later.

3.3 Properties of Polymer Solution

To simulate the flow, the viscosity and relaxation time of the polymer solution are needed for different polymer concentrations. Since, Polyox WSR301 is used in our experimental studies and is of interest in TVC suppression, we measured the total shear viscosity of Polyox solutions at different concentrations using the falling-ball method, i.e. the viscosity of liquid is deduced by measuring the terminal velocity of the falling ball based on the Stokes flow assumption. Rigorously speaking, the falling –ball method is only applicable to a Newtonian fluid. However, as suggested by Chhabra (1993), in the case of shear-thinning viscoelastic fluids, the drag on a sphere is largely determined by the shear dependent viscosity and that the viscoelasticity appears to exert little influence at least for small values of Deborah number. Therefore, we assume that the drag force which balances with the weight and buoyancy force in the falling-ball experiment is only caused by the total viscosity of the polymer solutions without any elasticity effect. Figure 15 shows the total viscosity at different polymer concentrations.

The relaxation time of Polyox WSR301 has been reported by Lindner et al. (2003) for concentration up to 1000 ppm. They found that in the dilute regime (less then 500 ppm) the relaxation time can be treated as constant (~0.0029 s) . However, another constant value (~0.0039 s) was found for the regime from 500 ppm to 1000 ppm. In this study, we set the relaxation time according to these two regimes.

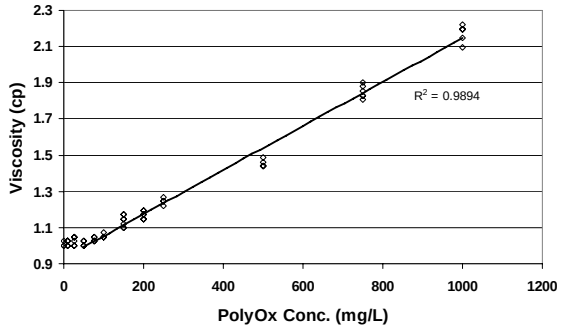

Figure 15. Shear viscosity of Polyox WSR301 solution at different concentrations measured with dropping ball method.

3.4 Propeller Tip Vortex Flow

We first applied the developed model to study the effect of polymers on cavitation suppression for a propeller tip vortex flow. We considered the DTMB Propeller 5168, a five-bladed propeller with a 15.86 inch (0.40 m) diameter. The flow field around this propeller was previously simulated by Hsiao and Pauley (1998). The simulation of the tip vortex flow was further improved by Hsiao and Chahine (2008) using a RANS-DNSS approach. This approach used RANS computations to obtain the overall flow field around the rotating propeller for high Reynolds number. The solution from the RANS computations was then improved by direct numerical simulation in reduced computation domain for which a much finer grid was generated to encompass the tip vortex roll-up and vortex sheet wake regions. Figure 16 shows the reduced domain used for the simulation of tip vortex flow.

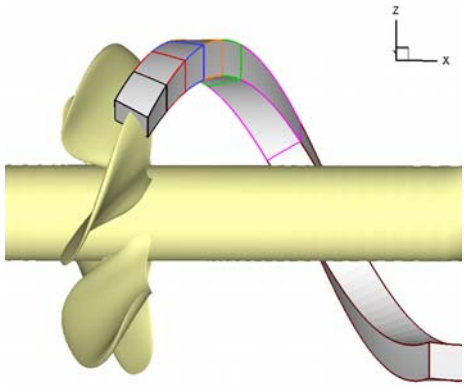

Figure 16. A view of the reduced computational domain used for the current computations.

In the present study, we use the same approach to simulate the tip vortex flow in a polymer solution. For the reduced domain computations, the boundary conditions were deduced from the RANS solution. The values of the pressures and velocities interpolated from the RANS solution are imposed at all reduced domain boundaries except for the inlet and outlet boundaries. At the inlet boundary the method of characteristics was applied with all three components of the velocity specified from the RANS solution. For the outlet boundary all the variables were extrapolated from the inner grid points. One should notice that by imposing the RANS (water) solution at the boundaries, we are imposing that the polymer effects only apply in the reduced domain, i.e. in the tip vortex centerline region. This corresponds to modeling artificially the case of polymer injection from the propeller blade tips. The tip vortex flows for water, 500 and 1,000ppm Polyox solutions were simulated using the parameters summarized in Table 2.

The propeller considered in this study had an advance coefficient, $J = 1.1$, which corresponds to a Reynolds number of of 4.19×10^6 based on:

$$R_e = \frac{\rho\sqrt{U_\infty^2 + (0.7\pi nD)^2}\,C_{0.7R}}{\mu}, \qquad (15)$$

where $C_{0.7R}$ is propeller blade chord length at the 0.7 radius section and μ is the water viscosity.

Concentration (ppm)	*J*	R_e	D_e	β
0	1.1	4.19×10^6	0	1.00
500	1.1	2.79×10^6	0.53	0.67
1000	1.1	2.10×10^6	0.53	0.50

Table 2: Parameters used in the simulations of the propeller tip vortex.

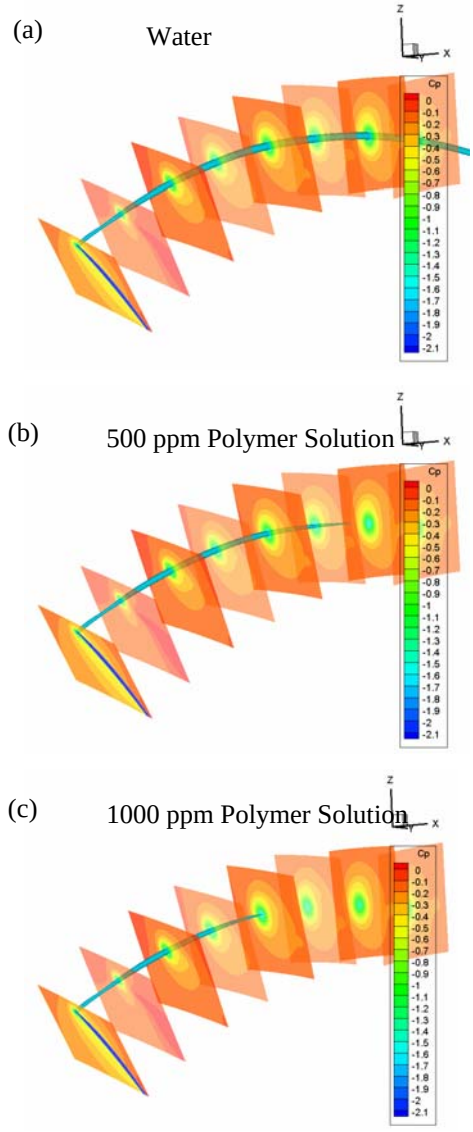

Figure 17. Iso-Cp surfaces (Cp=-1.6) equivalent to cavitation extent for: (a) water, (b) 500 ppm and (c) 1,000 ppm polymer solution.

Figure 17 shows the pressure coefficients contours in the tip vortex region for a) water, b) a 500 ppm solution of Polyox, and c) a 1,000 ppm solution of Polyox. As seen from the color levels, far from the vortex center (highest pressure region), the pressure fields for the water and the Polyox solution are very close. However, the pressures at the vortex center are noticeably lower for water than for the Polyox solutions. To illustrate the effect of polymer solutions on the evolution of the tip vortex cavitation shape , iso-Cp surfaces for the value of Cp corresponding to the negative cavitation number $\sigma = 1.6$ are also plotted and shown in Figure 17. This is similar to visualizing a cavitating vortex for different liquids at the same cavitation number. It is seen that in water a fully developed cavitation vortex core is observed to form from the tip of the blade and extend to the end of the domain. The extent of cavitating vortex becomes however much shorter as the polymer concentration is increased.

For a better comparison, the pressure coefficients along the vortex centerline are shown in Figure 18 for water, a 500 ppm Polyox solution, and a 1,000ppm Polyox solution. The results show that the overall pressure variations along the vortex centerline have the same trend for water and polymer solutions. In both cases, the pressure first decreases, reaches a minimum, and then increases. However, the presence of polymers makes the core pressure higher than that of water and the pressure returns faster to a higher value for a higher polymer concentration.

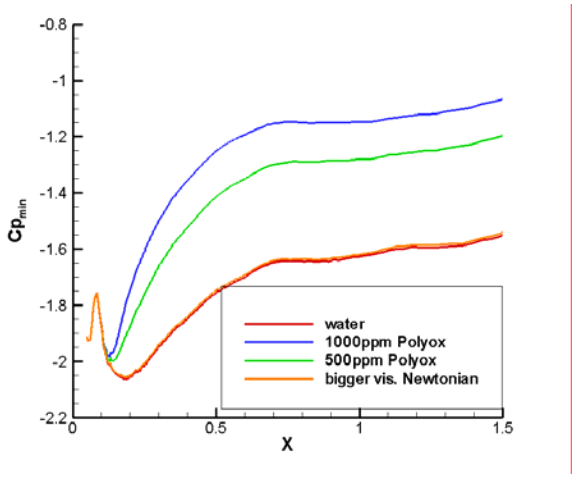

Figure 18. Comparison of the pressure coefficient variation along the vortex center. The lines in descending order are for 1000ppm Polyox, 500ppm Polyox, a Newtonian fluid with twice the viscosity of water, and water, respectively.

Since a polymer solution is more viscous than water, to investigate whether the pressure rise is due to

pure viscous or viscoelastic effects, we also simulated a Newtonian flow with a larger viscosity (twice that of water) and the pressure coefficient along the vortex is also shown in Figure 18. The difference between water and the twice-viscous fluid is small, indicating the strong importance of the non-Newtonian effects.

The trace of the polymer stress T and the pressure coefficient for the 1,000 ppm Polyox solution are shown together in Figure 19. We can see that following vortex roll-up close to the propeller tip, the polymer stress dramatically increases, reaches a maximum, then decreases steadily. The same trend was also found for the 500 ppm case. The fast increase of the polymer stresses correspond to stream-wise stretching of the vortex, which implies that stretch-induced normal stresses could be very important for the pressure rise.

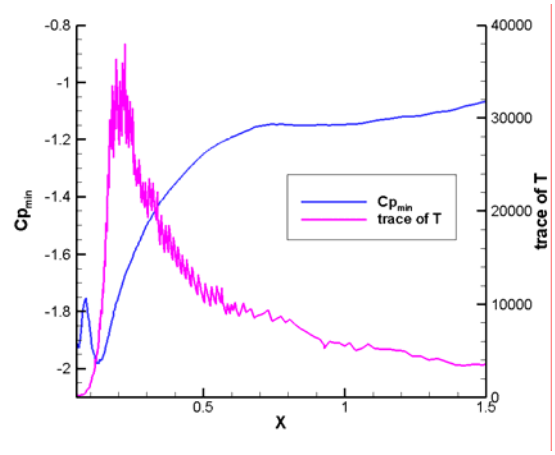

Figure 19. Pressure coefficient and the non-dimensional trace of polymer stress along the vortex center for the 1000ppm Polyox solution.

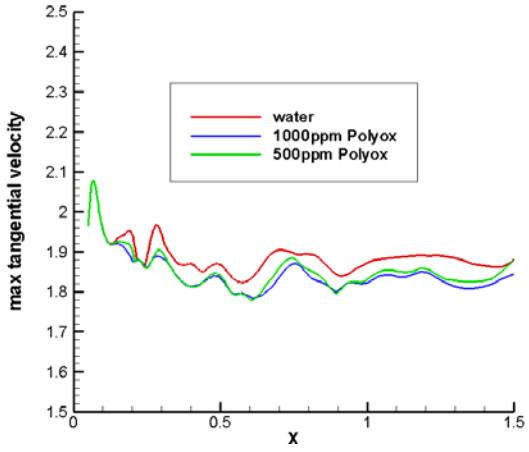

Figure 20. Maximal tangential velocity (non-dimensionalized with the free stream velocity) along the vortex.

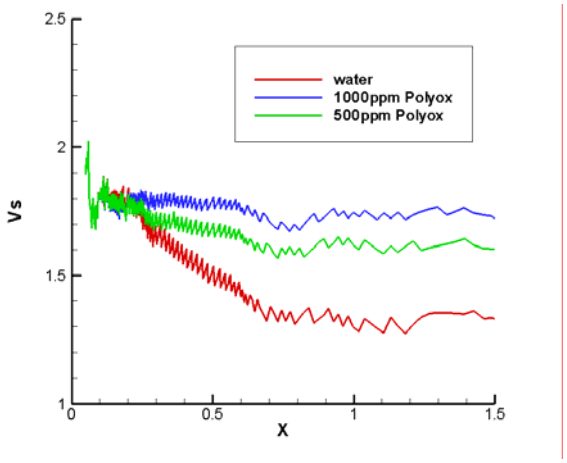

Figure 21. Velocity component parallel to the vorticity (non-dimensionalized with the free stream velocity) along the vortex center.

Figure 20 shows the maximal tangential velocity along the vortex. With polymer injected, the maximal tangential velocity becomes smaller, which is consistent with the pressure rise. The projection of the velocity along the vortex trajectory, V_s, at the vortex center is shown in Figure 21. It can be seen that polymer injection increases this velocity component. The higher the concentration is, the more the deviation from water is. This increase, however, appears to have less influence than the rotation speed on the pressure in the tip core.

3.5 Vortex Flow in the Swirl Chamber

The same polymer stress model was applied to simulate the vortex flow field in the swirl chamber described earlier in this paper. To fully resolve the flow field in the swirl chamber a very fine grid is required. For this study we consider the flow field as axially symmetric and thus neglect the three dimensional effects to speed up the numerical simulations and concentrate on the analysis of the polymer effect on the vortex flow. The 3D view of the fluid domain and the actual grid used for the simulation is shown in Figure 22. Inside the main chamber a 71x81 (radial by axial) stretched grid was used and for the orifice region a 16x31 grid was used. Near the chamber walls and the axis, much finer grids were used to capture the large velocity gradients.

The flow with a 6 gpm flowrate was studied. The Reynolds number based on water viscosity, orifice outlet diameter and average velocity at the outlet is 3.17×10^4. We simulated three cases: a) water b) chamber full of 500ppm polyox solution and c) local injection of 500ppm polyox from the end of the chamber. For all cases, a vortex forms at the chamber centerline and the velocities fluctuate with time. A

snapshot of the rotaional velocity is shown in Figure 23. Similar fluctuations show up in the experiments (see Figure 13). However, the present simulations cannot get the *exact* flow field as in the experiments due to the assumption of axisymmetry. Neverless, the simulations show qualitative consistency with the experiemnts. At this stage, we use the simulations to qualitatively study the polymer effects.

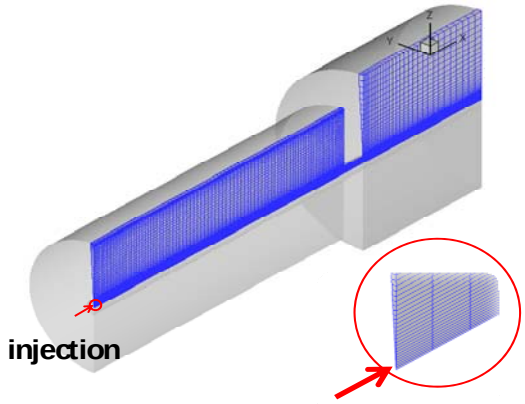

Figure 22. 3D view of the half domain and the grid mesh for the simulation of the vortex chamber flow.

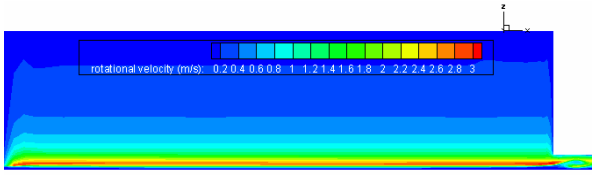

Figure 23. A snapshot of the rotational velocity contour inside the vortex chamber (water).

For the simulations of Case b, both the relaxtion time and viscosity of the polymer solutions was set to a constant value corresponding to 5000 ppm, However, for the simulation of Case c (the local polymer injection), the relaxtion time and viscosity are concentration-dependent. The relaxation time was set to either 0.0029 or 0.0039 sec according to the local concentration value. For the viscoisy, the viscosity-concentration relation shown in Figure 15 was used to account for concentration effects, i.e. the Reynolds number and β are computed locally according to the local polymer concentration. For this case, the 500ppm polyox solution is injected from the end of the chamber at a flowrate of $142cm^3 / \min$ and the polymer molecules are dispersed by the flow. Afer some time, as shown in Figure 24, the vortex is full of polymer solution .

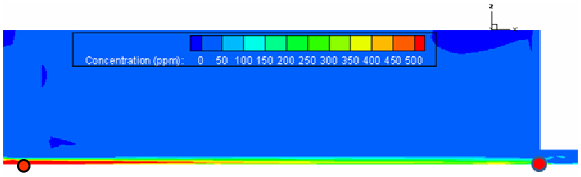

Figure 24. Contour of the polymer concentration in the vortex chamber. The red dots indicate the points where we monitor the pressure variation in time.

As the most important quantity related to the cavitation, the pressure evolution at points indicated in Figure 24 for the different simulated cases are compared in Figure 25. It is seen that for both polymeric flows, the pressure is higher than that of water and exhibits stronger oscillations and the local injection seems to have the same or even more efficient effect on the vortex pressure field.

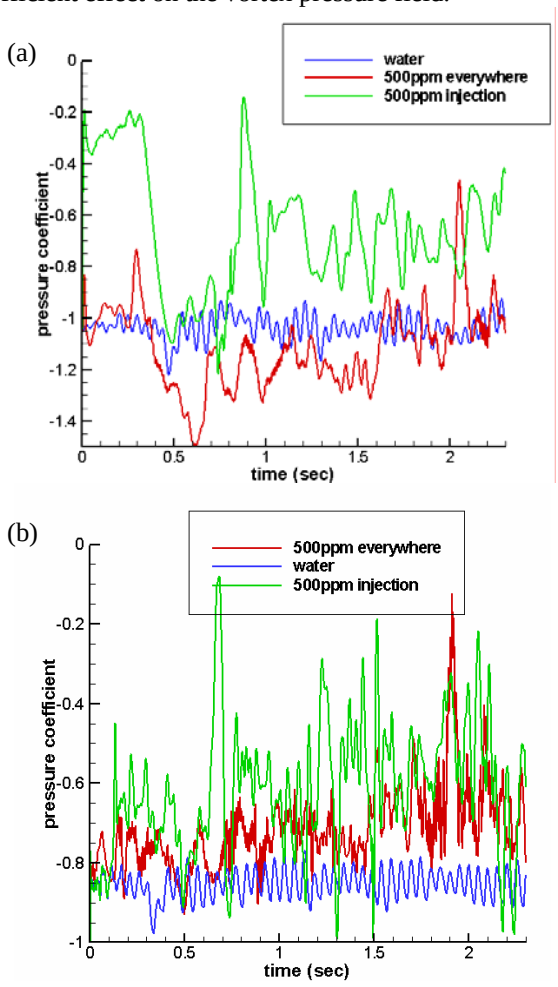

Figure 25. Evolution of the pressure coefficient at the monitored point (a) near the injection and (b) near outlet orifice for water only, 500ppm Polyox everywhere, and local injection of 500ppm Polyox.

4. Conclusions and Discussion

In this paper we presented both experimental and numerical studies of the effect of polymer injection on vortex cavitation. In the experimental study, the cavitation suppression could be observed directly while in the numerical study the resulting pressure field was used as an indication of cavitation suppression. .

In the experimental study it was found that plymer injection inhibits the occurrence of cavitation in the vortex core: for a given water flow rate and polymer concentration, there is a critical polymer injection rate, above which the cavitation core is destroyed. This critical injection rate decreases as the polymer concentration increases.

In the numerical study we have used a FENE-P model with our Navier-Stokes solver, 3DynaFS-Vis©. For propeller flow simulations with polymer solutions in the tip vortex centerline reduced domain, result in higher pressures at the vortex center than with pure water. Polymer stresses along the vortex centerline were found to increase dramatically and reach a maximum in the region close to the minimum pressure point. This is a purely viscoelastic effect, which was shown to not exist with a Newtonian flow with a larger viscosity.

The numerical simulation of the vortex flow in the swirl chamber has shown that the local injection of polymer increases the pressure along the vortex and thus would delay cavitation inception.

ACKNOWLEDGMNETS

This work was conducted at DYNAFLOW, INC. (*www.dynaflow-inc.com*) and was supported by the Office of Naval Research under contract No. N00014-08-C-0448 monitored by Dr. Ki-Han Kim.

REFERENCES

[1] Arabshahi, A., Taylor, L.K., Whitfield, D.L., "UNCLE: Toward a Comprehensive Time Accurate Incompressible Navier-Stokes Flow Solver, AIAA-95-0050, 1995.

[2] Barbier, C. and Chahine, G.L., "Experimental Study on the Effects of Viscosity and Viscoelasticity on a Line Vortex Cavitation", Proceedings of the 7th International Symposium on Cavitation, CAV2009, Ann Arbor, Michigan, 2009.

[3] Bird, R.B. Armstrong, R.C., and Hassager, O., "Dynamics of Polymeric Liquids," vol. 1&2, Wiley, New York, 1987.

[4] Chahine, G.L., Frederick, G.F. and Bateman, R.D., "Propeller Tip Vortex Cavitation Suppression Using Selective Polymer Injection", J. Fluid Egnr., **115**, pp.497-503, 1993.

[5] Chhabra, R.P., "Drops, and Particles in Non-Newtonian Fluids", CRC Press, Boca Raton, FL, 1993.

[6] Chorin, A. J., "A Numerical Method for Solving Incompressible Viscous Flow Problems," Journal of Computational Physics, **2**, pp. 12-26, 1967.

[7] Fruman, D. and Aflalo, S., "Tip Vortex Cavitation Inhibition by Drag Reducing Polymer Solution", J. Fluid Engr. **111**, pp.211-216, 1989.

[8] Fruman, D.H., Pichon, T. and Cerrutti, P., "Effect of a Drag-reducing Polymer Solution Ejection on Tip Vortex Cavitation", J. Mar. Sci. Tech., **1**, pp.13-23, 1995.

[9] Hsiao, C.-T., Pauley, L.L., "Numerical Computation of the Tip Vortex Flow Generated by a Marine Propeller," Journal of Fluids Engineering, **121**, No. 3, pp. 638-645, 1999.

[10] Hsiao, C.-T., Chahine, G.L., "Scaling of Tip Vortex Cavitation Inception for a Marine Open Propeller." 27th Symposium on Naval Hydrodynamics, Seoul, Korea, 5-10, Oct. 2008.

[11] Latorre, R., Muller, A., Billard, J.Y. and Houlier, A., "Investigation of the Role of Polymer on the Delay of Tip Vortex Cavitation", J. Fluid Engr., 126, pp.724-729, 2004.

[12] Li, C.F., Sureshkumar, R. and Khomami, B., "Influence of Rheological Parameters on Polymer Induced Turbulent Drag Reduction", J. Non-Newtonian Fluid Mech., **140**, pp23-40, 2006.

[13] Lindner, A., Vermant, J. and Bonn, D., "How to Obtain the Elongational Viscosity of Dilute Polymer Solutions", Physica A, 319, pp.125-133, 2003.

[14] Oliveira, P.J., Pinho, F.T. and Pinto, G.A., "Numerical Simulation of Non-linear Elastic Flows with a General Collocated Finite-volume Method", J. Non-Newtonian Fluid Mech., **7**9, pp1-43, 1998.

[15] Roe, P. L., "Approximate Riemann Solvers, Parameter Vectors, and Difference Schemes," Journal of Computational Physics, 43, pp. 357-372, 1981.

[16] White C. M. and Mungal, M. G. ,"Mechanics and Prediction of Turbulent Drag Reduction wuth Polymer Additives," Annu. Rev. Fluid. Mech. **40**, pp. 235-256, 2008.